Supplementary Information

Tailoring electronic structure to enhance ammonium-ion storage properties of VO₂ by molybdenum doping toward highly-efficient aqueous ammonium-ion battery

Yifu Zhang[1,2]*, Zhenhua Zhou[2], Xianfang Tan[1], Yanyan Liu[2], Fangfang Zhang[1], Changgong Meng[2], Xiaoming Zhu[1,]*

[1]*Hubei Key Laboratory of Radiation Chemistry and Functional Materials, School of Nuclear Technology and Chemistry & Biology, Hubei University of Science and Technology, Xianning 437100, P. R. China*
[2]*School of Chemistry, Dalian University of Technology, Dalian 116024, P. R. China*

*Corresponding authors.

E-mail address: yfzhang@dlut.edu.cn (Yifu Zhang); zhuxiaoming@hbust.edu.cn (Xiaoming Zhu)

1. Experimental section

1.1. Materials

The chemicals with analytical grade, including vanadium pentoxide (V_2O_5), ammonium molybdate, ammonium sulfate (($NH_4)_2SO_4$), hydrochloric acid (HCl), ammonium persulphate (($NH_4)_2S_2O_8$), aniline (ANI, purity > 99.0%), hydrogen peroxide (H_2O_2, 30 wt.%) and ethanol, were purchased from Sinopharm Chemical Reagent Co., Ltd. and used without any further purification.

1.2. Synthesis of VO_2 and VO_2-Mo

In a typical synthesis, commercial V_2O_5 (0.455 g) and a certain amount of ammonium molybdate (the mole amount of molybdate was adjusted to be 1.0 %, 2.0 % and 4.0 %) were added to 28 mL of distilled water. Subsequently, 3 mL of H_2O_2 was added and stirred for 0.5 h. After an orange solution is formed, 5 mL of anhydrous ethanol was added and the stirring was continued for 10 min, and then the above mixture was transferred to a 50 mL PTFE-lined autoclave, sealed and heated up to 180 °C for 72 hours. After the reaction, it was cooled to the room temperature naturally. The samples were collected by filtering off, washing with distilled water and absolute ethanol several times and drying in vacuum at 75 °C to obtain molybdenum doped vanadium dioxide (denoted as VO_2-Mo).

The pure VO_2 was synthesized with the same as the VO_2-Mo without the presence of ammonium molybdate. The usage of ($NH_4)_2MoO_4$ is crucial for controlling the NH_4^+ storage properties of the material, and we introduced ($NH_4)_2MoO_4$ with masses of 0, 0.009, 0.018, and 0.036 g to obtain four samples with different doping amounts of VO_2, VO_2-Mo (1%), VO_2-Mo (2%), and VO_2-Mo (4%), respectively.

1.3. Synthesis of PANI

In a typical synthesis of the polyaniline (PANI) as the cathode material [1], 0.365 mL of aniline solution was added to 15 mL of 1 M HCl solution to obtain solution A, which was stirred in an ice-water bath for 1 h. 0.228 g of ($NH_4)_2S_2O_8$ was dissolved in 5 mL of HCl to obtain solution B, which was finally added dropwise to solution A and reacted for 1 h in an ice-water bath to obtain the PANI.

1.4. Materials characterizations

The crystal structure information of the samples was analyzed on the X-ray powder diffractometer (Bruker, D8 Advance) equipped with Cu Kα radiation (λ=1.5418 Å) and Confocal micro-Raman Spectrometer (Raman, inVia Qontor, Renishaw). Fourier transform infrared (FTIR) spectroscopy of the solid samples was conducted on Nicolet 6700 spectrometer using KBr pellet technique from 4000 to 400 cm^{-1} with a resolution of 4 cm^{-1}. About 1 wt% of the samples and 99 wt% of KBr were mixed homogeneously, and then the mixture was pressed to a pellet. The electron paramagnetic resonance (EPR) spectra were performed on EMX-Micro (Bruker, German). The surface elements valence states and chemical composition were performed on an X-ray photoelectron spectroscopy (XPS) spectrometer (Shimadzu, Axis Supra$^+$) with the excitation source of Al Kα X-ray radiation. The morphologies of the materials were observed by a field emission scanning electron microscope (FE-SEM, NOVA NanoSEM 450, FEI) and field emission transmission electron microscope (TEM, FEITecnai F30, FEI). Energy dispersive spectroscopy (EDS) and elemental mapping were done using the field emission scanning electron microscope (FE-SEM, NOVA NanoSEM 450, FEI). Micromeritics ASAP-2020 was employed to record the pore information based on Brunauer-Emmett-Teller (BET) theory and the Barrett-Joyner-Halenda (BJH) method, which was degassed at 130 ℃.

1.5. Electrochemical measurements

A homogeneous slurry was formed by mixing the active material, acetylene black, and polyvinylidene fluoride (PVDF) in N-methyl-2-pyrrolidone (NMP) at the mass ratio of 7:2:1. The slurry was coated onto Ti foil and dried under vacuum at 60 ℃ overnight to prepare the working electrodes. The active material mass loading was about 2 mg·cm^{-2}, and all measurements were taken at room temperature. For single electrode performances, electrochemical tests were performed in the three-electrode system constructed by the working electrode, Ag/AgCl reference electrode, and active carbon as counter electrode. Aqueous 1 M $(NH_4)_2SO_4$ solution was used as electrolyte to study the NH_4^+ storage mechanism. To explore the practicability of the material, full cells were assembled using VO_2-Mo as the anode, PANI as the cathode and 1 M $(NH_4)_2SO_4$ as the electrolyte assembled in standard CR2032 coin cell. In both single electrode system and full cell, cyclic voltammetry (CV) and electrochemical impedance spectroscopy (EIS) (0.01-100 kHz) tests were conducted using the CHI-660D electrochemical workstation, while the galvanostatic charge-discharge (GCD) were carried out using LAND CT2001A.

1.6. Theoretical calculation method

All the geometric optimizations, single-point energies and electronic structures calculations are performed through the spin-polarized density functional theory method by using the Cambridge Serial Total Energy Package (CASTEP) code on the basis of the plane-wave pseudopotential. The Perdew-Burke-Ernzerhof (PBE) exchange-correlation functional for generalized gradient approximation (GGA) and the projector augmented wave (PAW) method explaining the core-valence interactions are employed. The valence electrons were expanded in a plane-wave basis set within a cutoff energy of 500 eV. The electronic relaxation is performed to within an energy tolerance of 2×10^{-5} eV for self-consistency, while ionic optimizations are performed until all the residual forces are smaller than 0.05 eV/Å. Monkhorst-Pack meshes with $1\times1\times1$ k-points were used to sample the Brillouin zone of VO_2 and VO_2-Mo calculations, respectively. The adsorption energies were calculated on the VO_2 and VO_2-Mo (1 0 0) plane using a 7.44×6.58 Å^2 cell with an at least 15 Å vacuum along the c axis to separate the slabs. For the calculation of adsorption energies, single gamma-point grid was used. The force acting on each atom converged to 0.004 Ha·Å^{-1} and the energy criterion was set to $2*10^{-5}$ Ha.
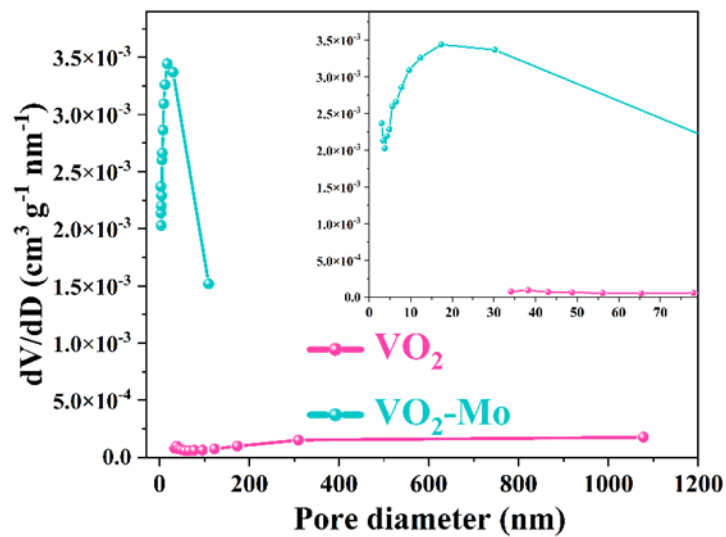
Figures

Figure S1

Figure S1. Pore size distribution based on Barrett-Joyner-Halenda (BJH) method using the adsorption
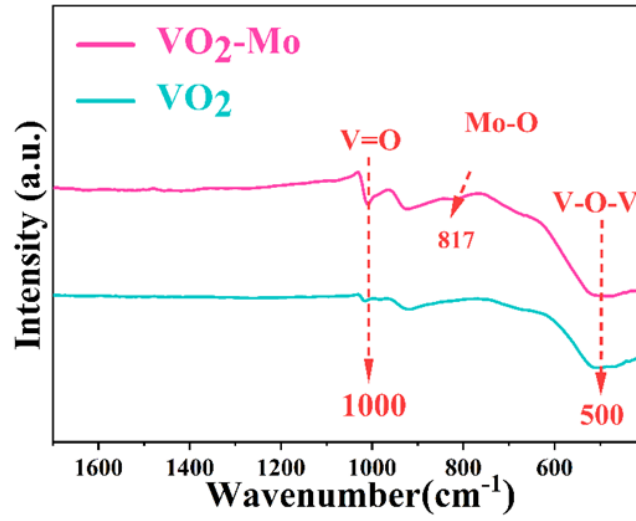
isotherms of VO_2 and VO_2-Mo.

Figure S2
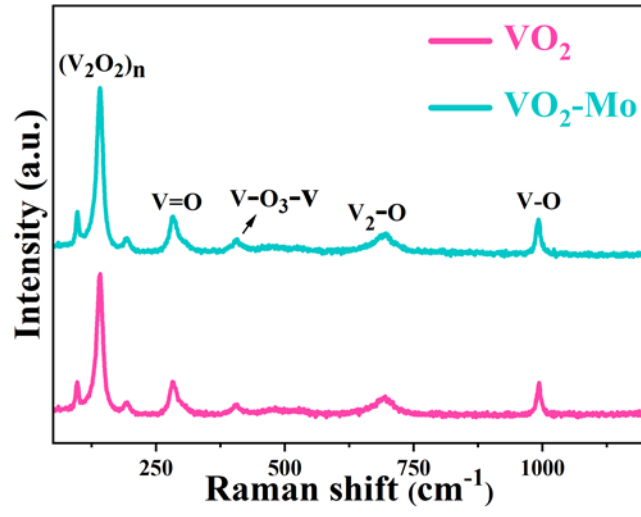

Figure S2. FTIR spectra of VO_2 and VO_2-Mo.

Figure S3

Figure S3. Raman spectra of VO_2 and VO_2-Mo.

Figure S4
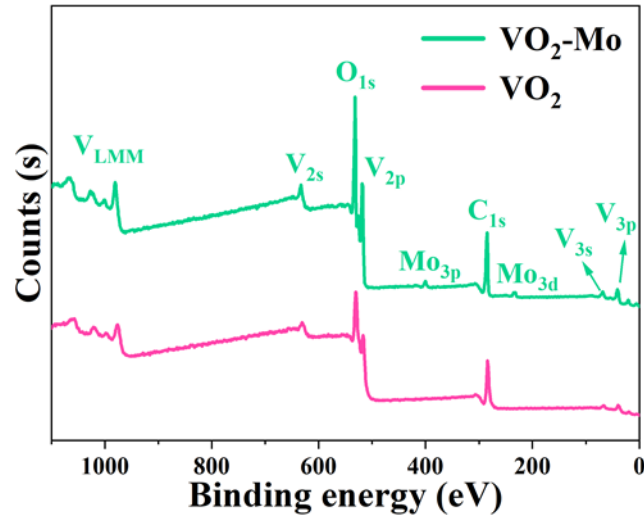
Figure S4. Full XPS spectra of VO_2 and VO_2-Mo.

Figure S5
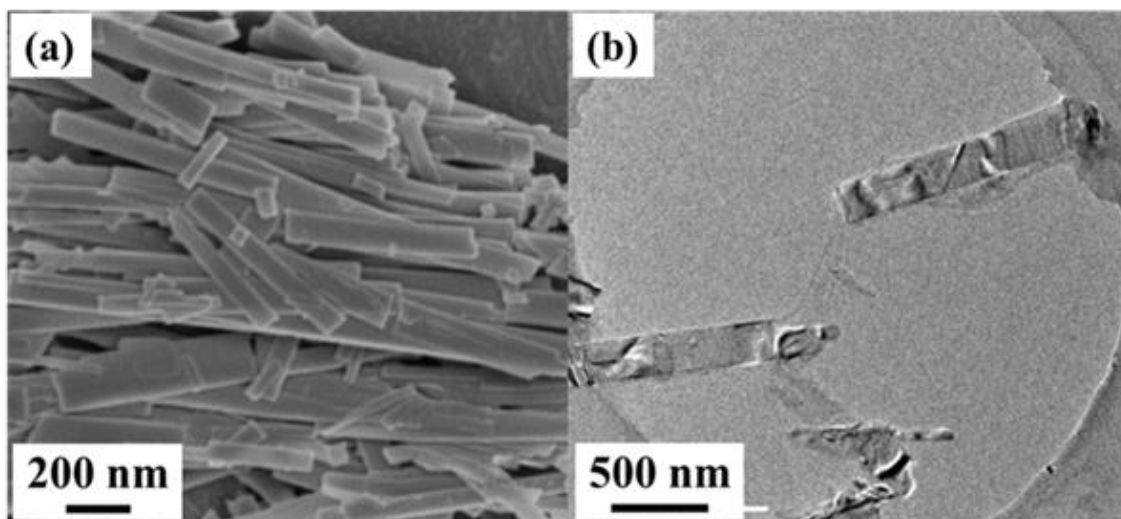
Figure S5. (a) SEM image of VO_2; (b) TEM image of VO_2.
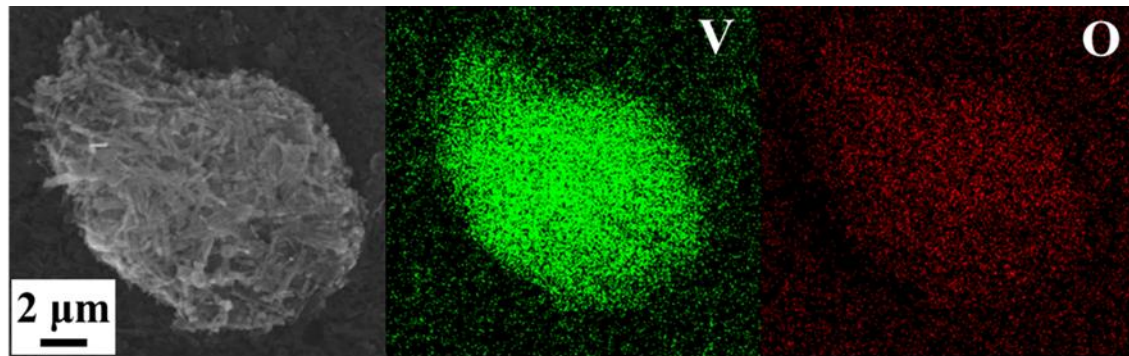
Figure S6

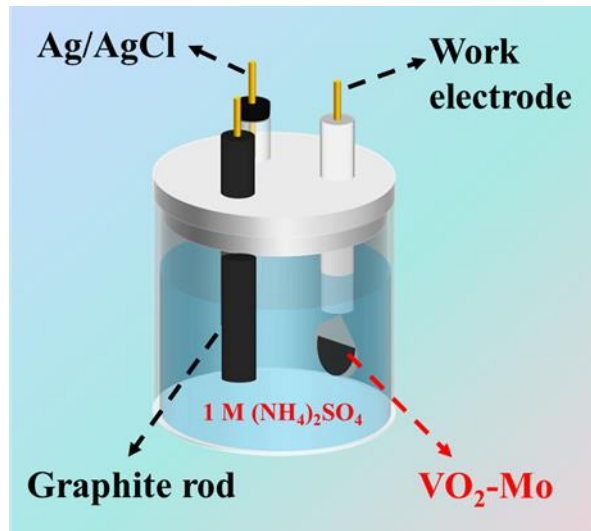**Figure S6.** Elemental mapping images of VO_2.

Figure S7

Figure S7. Three-electrode configuration for evaluating the electrochemical properties of VO_2 and VO_2-Mo for ammonium-ion storage.
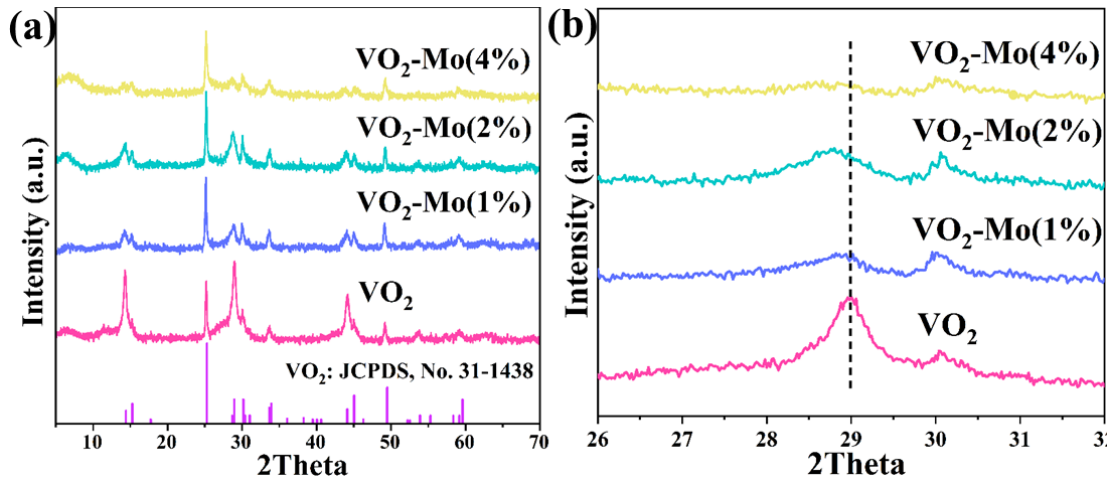
Figure S8

Figure S8. XRD patterns of VO_2 and VO_2-Mo with different content of Mo doping: (a) A large range 2θ;

(b) A small range 2θ.
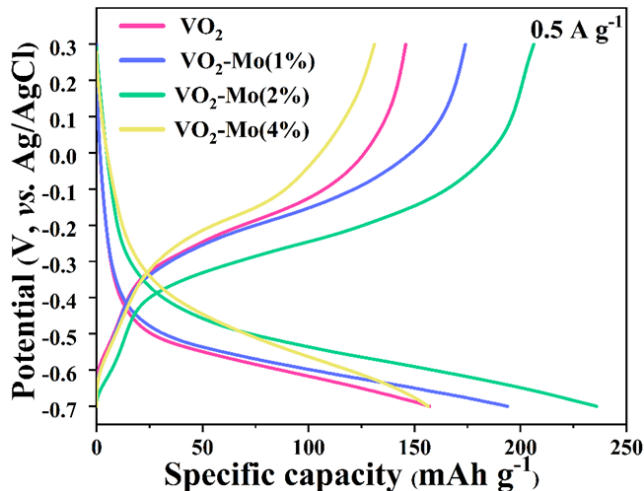
Figure S9

Figure S9. GCD curves of VO_2 and VO_2-Mo with different content of Mo doping (**Figure S8**) to show its influence on ammonium-ion storage properties.

To study the influence of the amount of Mo in VO_2 on its electrochemical properties, the mole amount of ammonium molybdate was adjusted to be 0, 1.0 %, 2.0 % and 4.0 % based on the following equation (S1):

$$Percentage\ (\%) = [n(Mo)/n(V+Mo)*100\% \qquad (S1)$$

These corresponding samples were named as VO_2, VO_2-Mo(1%), VO_2-Mo(2%) and VO_2-Mo(4%), respectively.

The galvanostatic charge-discharge (GCD) curves of these samples at 0.5 A g^{-1} are shown in Figure S9 (**Supplementary Material**), which proves that the most significant performance enhancement of VO_2 that is achieved at a Mo content of 2 %. In detail, with the Mo mole ratio from 0 to 1.0 %, 2.0 % and 4.0 %, the specific capacities are measured from 152 mAh g^{-1} to 184 mAh g^{-1}, 222 mAh g^{-1} and 144 mAh g^{-1}, respectively. VO_2 with 2% Mo-doping exhibits the best electrochemical properties for NH_4^+-storage among these samples. In this work, for convenience, we use the VO_2-Mo representing Mo-doped VO_2-Mo(2%) in the whole article.
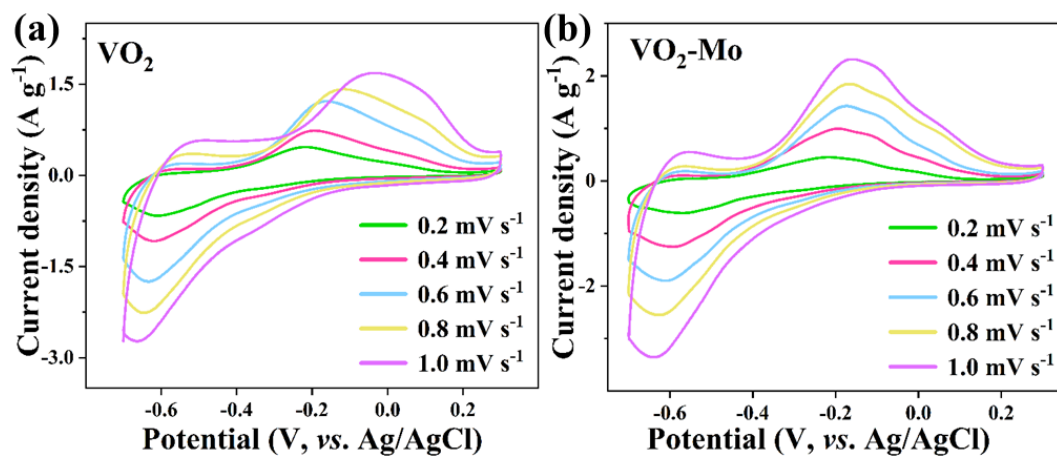
Figure S10

Figure S10. (a) CV curves of VO_2 at different scan rates; (b) CV curves of VO_2-Mo at different scan
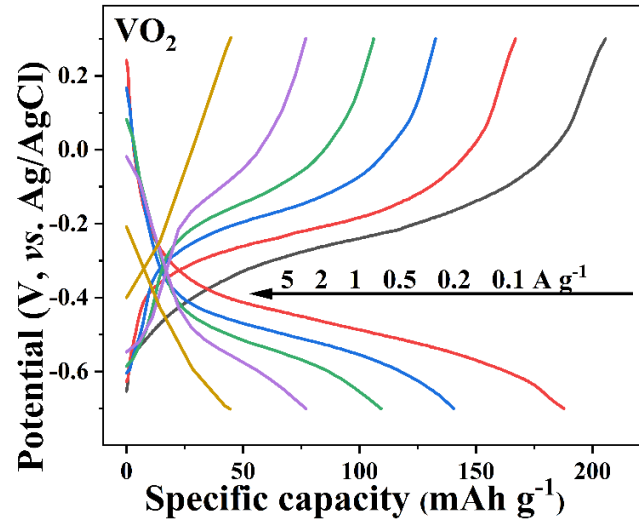
rates.

Figure S11

Figure S11. GCD curves of VO_2 at different current densities.
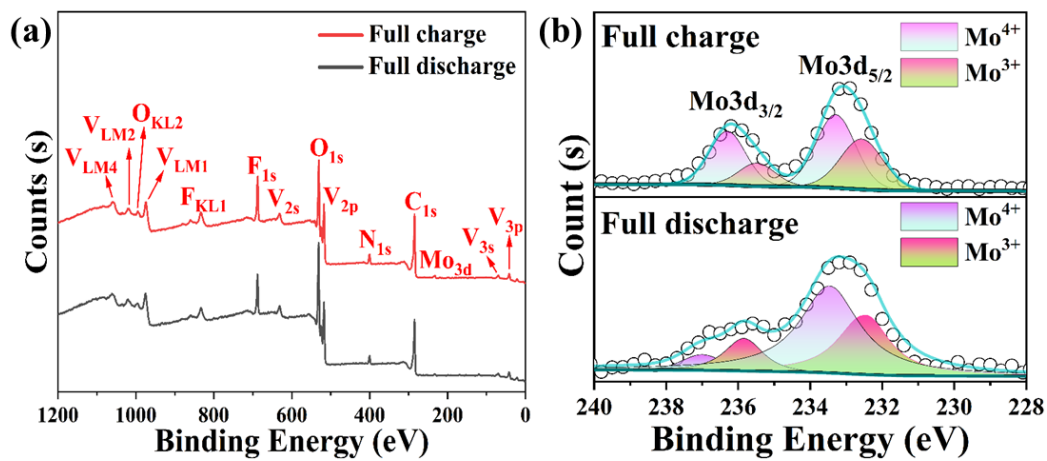
Figure S12

Figure S12. (a) Full XPS spectra during full charge and full discharge; **(b)** XPS spectra of Mo3d during full charge and full discharge.

Figure S13
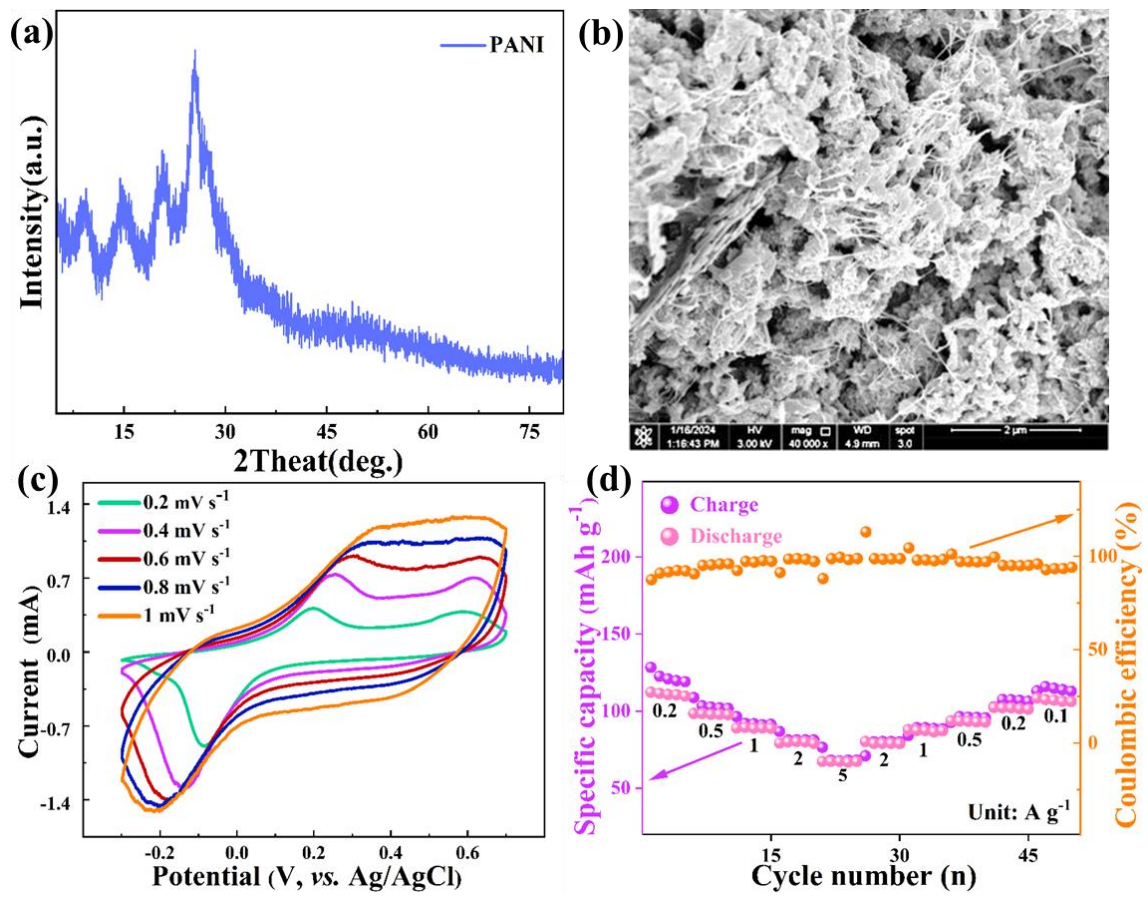
Figure S13. Characterization and electrochemical properties of PANI: (a) XRD pattern; (b) SEM image; (c)

CV curves at different scan rates; (d) Rate performances at different current densities.

Figure S14
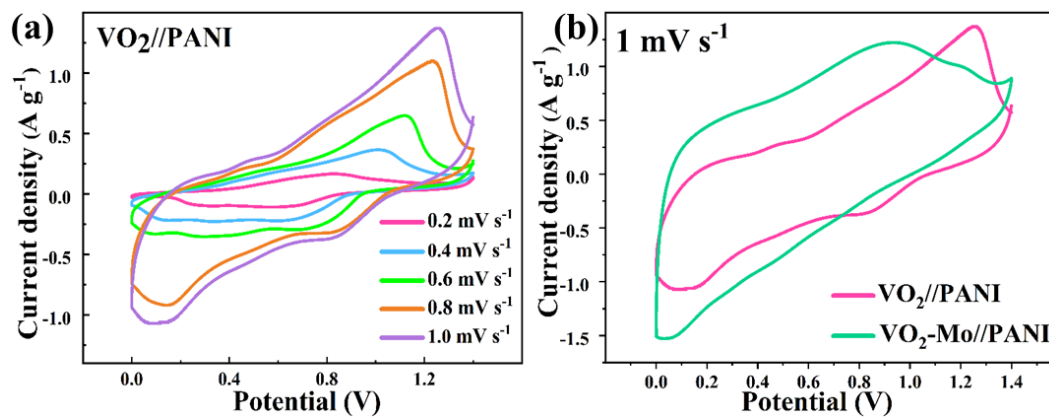
Figure S14. (a) CV curves of VO$_2$//PANI at different scan rates; (b) Comparison of CV curves of VO$_2$-Mo//PANI and VO$_2$//PANI batteries at 1 mV s^{-1}.

5Figure S15
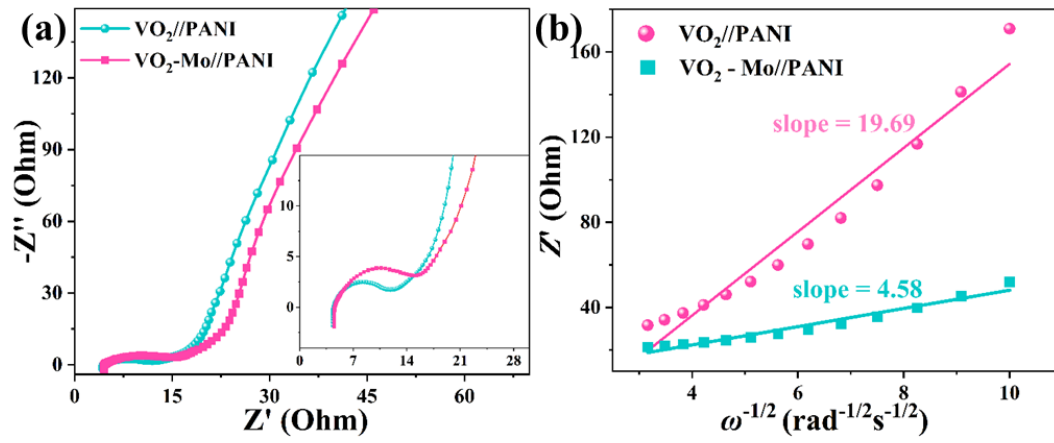
Figure S15. (a) Nyquist plots and (b) Fitting of Z'-$\omega^{-1/2}$ curves of VO_2//PANI and VO_2-Mo//PANI.

Figure S16

Figure S16. (a) DOS of VO_2 and VO_2-Mo; (b-c) PDOS of O2p and V3d of VO_2 and VO_2-Mo.

Figure S17

Figure S17. The structural models of (a) VO_2 and (b) VO_2-Mo for calculating the adsorption energy with ammonium ion.

Table S1

Table S1. Comparison of electrochemical properties of VO_2 and VO_2-Mo for NH_4^+ storage compared with other materials for NH_4^+ storage reported in previous researches.
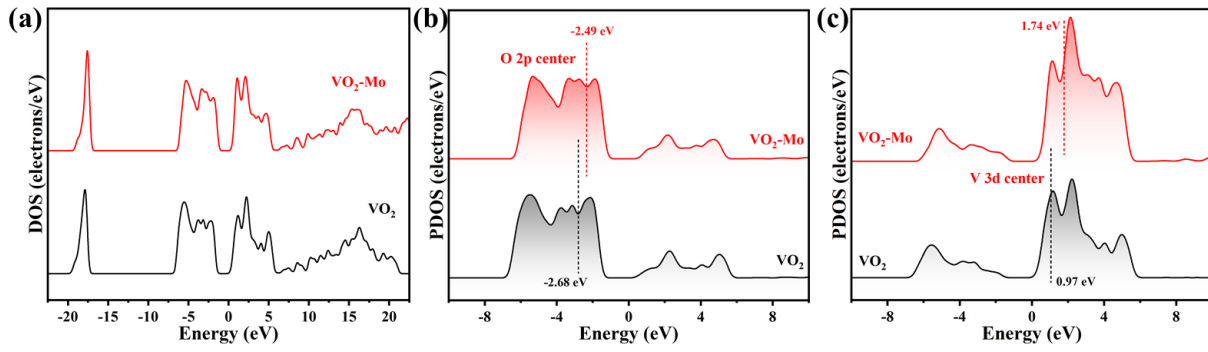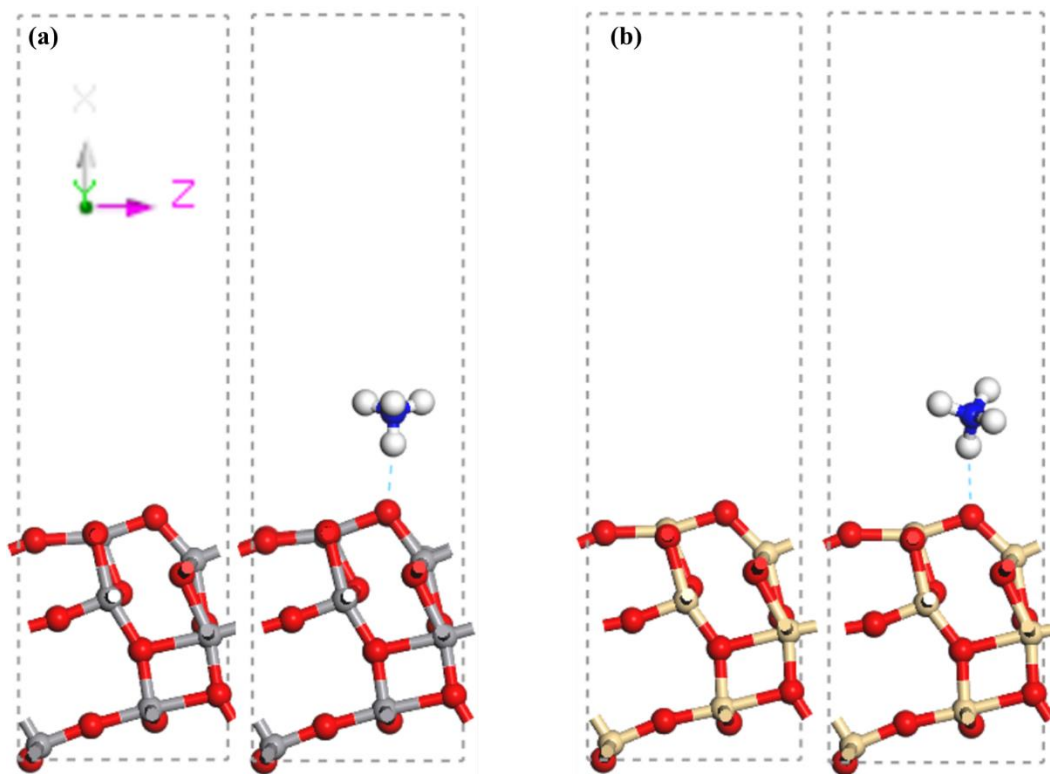
Materials	Electrolyte	Specific capacity, current density	Ref.
VO_2-Mo	1 M $(NH_4)_2SO_4$	~370 mAh·g^{-1}@0.1 A·g^{-1}	This work
VO_2	1 M $(NH_4)_2SO_4$	~232 mAh·g^{-1}@0.1 A·g^{-1}	This work
d-VO nanoribbon	1 M $(NH_4)_2SO_4$	~200 mAh·g^{-1}@0.1 A·g^{-1}	[2]
d-HVO-2	1 M $(NH_4)_2SO_4$	220 mAh·g^{-1}@0.1 A·g^{-1}	[3]
$VOPO_4·2H_2O$	1 M NH_4OTf	154.6 mAh·g^{-1}@0.1 A·g^{-1}	[4]
VS_2	5 M $(NH_4)_2SO_4$	120 mAh·g^{-1}@0.1 A·g^{-1}	[5]
FVO	1 M $(NH_4)_2SO_4$	88.6 mAh·g^{-1}@0.1 A·g^{-1}	[6]
$NH_4V_4O_{10}$	1 M $(NH_4)_2SO_4$	167 mAh·g^{-1}@0.1 A·g^{-1}	[7]
Berlin Green	0.5 M $(NH_4)_2SO_4$	90 mAh·g^{-1}@0.1 A·g^{-1}	[8]
MoO_3	1 M NH_4Cl	115 mAh·g^{-1}@0.1 A·g^{-1}	[9]
MnOx	0.5 M NH_4Ac	176 mAh·g^{-1}@0.5 A·g^{-1}	[10]
$NaFe_{III}Fe_{II}(CN)_6$	1 M $(NH_4)_2SO_4$	62 mAh·g^{-1}@0.25 A·g^{-1}	[11]
MnAl-LDH	0.5 M $(NH_4)_2SO_4$	84 mAh·g^{-1}@0.1 A·g^{-1}	[12]
CuHCF	0.5 M $(NH_4)SO_4$	60 mAh·g^{-1}@0.1 A·g^{-1}	[13]
Titanic acid	25 M AmAc	84 mAh·g^{-1}@1 A·g^{-1}	[14]

Table S2

Table S2. Comparison of the electrochemical performances of the VO$_2$@C‖PANI full battery in this work with some reported batteries.

Batteries (devices)	Electrolyte	Energy density	Power density	Ref.
VO$_2$@C‖PANI	(NH$_4$)$_2$SO$_4$	160 Wh kg^{-1}	168 W kg^{-1}	This work
MnO$_2$//d-VO	(NH$_4$)$_2$SO$_4$	96.1 Wh kg^{-1} 26 Wh kg^{-1}	51.4 W kg^{-1} 3254 Wh kg^{-1}	[2]
MnAlLDH//PTCDI	(NH$_4$)$_2$SO$_4$	45.8 Wh kg^{-1}	163.5 Wh kg^{-1}	[12]
MoO$_3$@C//MoO$_3$@C	(NH$_4$)$_2$SO$_4$	78.3 Wh kg^{-1}	929.1 Wh kg^{-1}	[15]
MoO$_3$//CuFe PBA	PAM hydrogel	21.3 Wh kg^{-1}	277 Wh kg^{-1}	[9]
NVO//AC	NH$_4$Cl/PVA	15.9 Wh kg^{-1}	9.16 W kg^{-1}	[16]
PVO//AC	NH$_4$Cl/PVA	17.5 Wh kg^{-1}	25.4 W kg^{-1}	[17]
ACC@VPP//PTCDI	NH$_4$Cl/PVA	10.6 Wh kg^{-1}	28.9 Wkg^{-1}	[18]
VOH/PEDOT//AC	NH$_4$Cl/PVA	10.4 Wh kg^{-1}	35.7 W kg^{-1}	[19]
KVO/PANI//AC	NH$_4$Cl/PVA	31.8 Wh kg^{-1}	47.6 W kg^{-1}	[20]

PVA = Polyvinyl Alcohol.

References

[1] S.F. Kuchena, Y. Wang, Superior Polyaniline Cathode Material with Enhanced Capacity for Ammonium Ion Storage, ACS Appl. Energy Mater. 3 (2020) 11690-11698.

[2] Y. Wu, S. Dong, N. Lv, Z. Xu, R. Ren, G. Zhu, B. Huang, Y. Zhang, X. Dong, Unlocking the High Capacity Ammonium-Ion Storage in Defective Vanadium Dioxide, Small 18 (2022) 2204888.

[3] J.n. Gong, P. Bai, J. Sun, Y. Liu, X. Dong, T. Hu, C. Meng, Y. Zhang, Adjusting oxygen vacancy of $VO_2 \cdot xH_2O$ nanoarray architectures for efficient NH_4^+ storage, Nano Res. 17 (2024) 2646-2654.

[4] F. Ye, R. Pang, C. Lu, Q. Liu, Y. Wu, R. Ma, L. Hu, Reversible Ammonium Ion Intercalation/de-intercalation with Crystal Water Promotion Effect in Layered $VOPO_4 \cdot 2H_2O$, Angew. Chem. Int. Ed. 62 (2023) e202303480.

[5] D. Yu, Z. Wei, X. Zhang, Y. Zeng, C. Wang, G. Chen, Z.X. Shen, F. Du, Boosting Zn^{2+} and NH_4^+ Storage in Aqueous Media via In-Situ Electrochemical Induced VS_2/VO_x Heterostructures, Adv. Funct. Mater. 31 (2021) 2008743.

[6] W. Xu, L. Zhang, K. Zhao, X. Sun, Q. Wu, Layered ferric vanadate nanosheets as a high-rate NH_4^+ storage electrode, Electrochim. Acta 360 (2020) 137008.

[7] H. Li, J. Yang, J. Cheng, T. He, B. Wang, Flexible aqueous ammonium-ion full cell with high rate capability and long cycle life, Nano Energy 68 (2020) 104369.

[8] X. Wu, Y. Xu, H. Jiang, Z. Wei, J.J. Hong, A.S. Hernandez, F. Du, X. Ji, NH_4^+ Topotactic Insertion in Berlin Green: An Exceptionally Long-Cycling Cathode in Aqueous Ammonium-Ion Batteries, ACS Appl. Energy Mater. 1 (2018) 3077-3083.

[9] G. Liang, Y. Wang, Z. Huang, F. Mo, X. Li, Q. Yang, D. Wang, H. Li, S. Chen, C. Zhi, Initiating Hexagonal MoO_3 for Superb-Stable and Fast NH_4^+ Storage Based on Hydrogen Bond Chemistry, Adv. Mater. 32 (2020) e1907802.

[10] Y. Song, Q. Pan, H. Lv, D. Yang, Z. Qin, M.Y. Zhang, X. Sun, X.X. Liu, Ammonium-Ion Storage Using Electrodeposited Manganese Oxides, Angew. Chem. Int. Ed. 60 (2021) 5718-5722.

[11] C. Li, W. Yan, S. Liang, P. Wang, J. Wang, L. Fu, Y. Zhu, Y. Chen, Y. Wu, W. Huang, Achieving a high-performance Prussian blue analogue cathode with an ultra-stable redox reaction for ammonium ion storage, Nanoscale Horiz. 4 (2019) 991-998.

[12] Q. Liu, F. Ye, K. Guan, Y. Yang, H. Dong, Y. Wu, Z. Tang, L. Hu, MnAl Layered Double Hydroxides: A Robust Host for Aqueous Ammonium-Ion Storage with Stable Plateau and High Capacity, Adv. Energy Mater. 13 (2023) 2202908.

[13] C.D. Wessells, S.V. Peddada, M.T. McDowell, R.A. Huggins, Y. Cui, The Effect of Insertion Species on Nanostructured Open Framework Hexacyanoferrate Battery Electrodes, J. Electrochem. Soc. 159 (2011) A98-A103.

[14] J.J. Holoubek, H. Jiang, D. Leonard, Y. Qi, G.C. Bustamante, X. Ji, Amorphous titanic acid electrode: its electrochemical storage of ammonium in a new water-in-salt electrolyte, Chem. Commun. 54 (2018) 9805-9808.

[15] J. Dai, X. Qi, L. Xia, Q. Xue, L. Luo, X. Wang, C. Yang, D. Li, H. Xie, A. Cabot, L. Dai, Y. Xu, Aqueous Ammonium-Ion Supercapacitors with Unprecedented Energy Density and Stability Enabled by Oxygen Vacancy-Enriched MoO3@C, Adv. Funct. Mater. 33 (2023) 2212440.

[16] P. Wang, Y. Zhang, H. Jiang, X. Dong, C. Meng, Ammonium vanadium oxide framework with stable NH_4^+ aqueous storage for flexible quasi-solid-state supercapacitor, Chem. Eng. J. 427 (2022) 131548.

[17] P. Wang, Y. Zhang, Z. Feng, Y. Liu, C. Meng, A dual-polymer strategy boosts hydrated vanadium oxide for ammonium-ion storage, J. Colloid Interface Sci. 606 (2022) 1322-1332.

[18] X. Chen, P. Wang, Z. Feng, C. Meng, Y. Zhang, Conductive polymer intercalated vanadium oxide on carbon cloth for fast ammonium-ion storage in supercapacitor applications, Chem. Eng. J. 445 (2022) 136747.

[19] X. Chen, P. Wang, Z. Feng, Y. Liu, M. Cui, C. Meng, Y. Zhang, Structural regulation of vanadium oxide by poly(3,4-ethylenedioxithiophene) intercalation for ammonium-ion supercapacitors, Adv. Sensor Energy Mater. 1 (2022) 100013.

[20] X. Chen, Z. Feng, X. Dong, H. Jiang, C. Meng, Y. Zhang, Synergistic effect of K+ and PANI in vanadium oxide hydration by interlayer engineering boosts the ammonium ion storage, SusMat 3 (2023) 263-275.